Research
Civil Engineering—Article

Field Observations of Near-Surface Wind Flow Across Expressway Embankment on the Qinghai–Tibet Plateau

Yanhu Mu [a,b], Wei Ma [a,b,*], Zhaohui (Joey) Yang [c,*], Xiaolin Li [d], Kun Zhang [e], Yuncheng Mao [e]

[a] State Key Laboratory of Frozen Ground Engineering, Northwest Institute of Eco-Environment and Resources, Chinese Academy of Sciences, Lanzhou 730000, China
[b] University of Chinese Academy of Sciences, Beijing 100049, China
[c] College of Engineering, University of Alaska Anchorage, Anchorage, AK 99508, USA
[d] College of Civil Engineering and Architecture, Jiaxing University, Jiaxing 314001, China
[e] School of Civil Engineering, Northwest Minzu University, Lanzhou 730024, China

ARTICLE INFO

ABSTRACT

Crushed rock layers (CRLs), ventilation ducts (VDs) and thermosyphons are air-cooling structures (ACSs) widely used for maintaining the long-term stability of engineered infrastructures in permafrost environments. These ACSs can effectively cool and maintain the permafrost subgrade's frozen state under climate warming by facilitating heat exchange with ambient air in cold seasons. As convection is a crucial working mechanism of these ACSs, it is imperative to understand the near-surface wind flow (NSWF) across a constructed infrastructure, such as an embankment. This article describes a yearlong field observation of the NSWF across an experimental expressway embankment, the first of its kind on the Qinghai–Tibet Plateau (QTP). The wind speed and direction along a transect perpendicular to the embankment on both the windward and leeward sides and at four different heights above the ground surface were collected and analyzed. The results showed that the embankment has a considerable impact on the NSWF speed within a distance of up to ten times its height, and in the direction on the leeward side. A power law can well describe the speed profiles of NSWF across the embankment, with the power-law indices (PLIs) varying from 0.14 to 0.40. On an annual basis, the fitted NSWF PLI far away from the embankment was 0.19, which differs substantially from the values widely used in previous thermal performance evaluations of ACSs on the QTP. Finally, the significance of the NSWF to the thermal performance of the ACSs, particularly the CRLs and VDs, in linear transportation infrastructure is discussed. It is concluded that underestimating the PLI and neglecting wind direction variations may lead to unconservative designs of the ACSs. The results reported in this study can provide valuable guidance for infrastructure engineering on the QTP and other similar permafrost regions.

1. Introduction

One-quarter of the Northern Hemisphere and 17% of Earth's exposed land surface are underlain by permafrost [1]. These vast permafrost regions play an important role in the world economy due to their rich natural resources, including an estimated 25% of the world's undiscovered oil and gas reserves [2,3]. In recent decades, economic development has resulted in an extensive expansion of hydrocarbon extraction, transportation networks, communication lines, industrial projects, civil facilities, and

engineering maintenance systems in permafrost regions [4]. However, ongoing climate warming and consequent permafrost degradation have severely damaged thousands of infrastructure components and led to significant economic losses [5–10]. The most recent assessments show that by 2050, 33% of the infrastructure built in the Northern Hemisphere's permafrost regions will experience damage from ground subsidence and loss of structural bearing capacity induced by permafrost degradation [11]. Thus, how to economically maintain the existing infrastructure and scientifically construct future infrastructures on degrading permafrost is a great engineering challenge. It is critical to regulate heat exchange between a permafrost foundation and the ambient environment because the permafrost thermal regime is a key

* Corresponding authors.
E-mail addresses: mawei@lzb.ac.cn (W. Ma), zyang2@alaska.edu (Z. (J.) Yang).

variable that determines the bearing capacity and deformation behaviors of foundations [12–14].

Construction activity affects the natural ground surface conditions and the ground thermal regime by changing the energy exchange between the ground and the atmosphere. For permafrost roadway embankments, such an impact can be substantial as great changes in material properties, surface albedo, super-permafrost hydrology and vegetation covers can occur during embankment construction and operation. High-porosity crushed rock layers (CRLs), ventilation ducts (VDs) and thermosyphons have been proven to be effective air-cooling structures (ACSs) for maintaining the long-term thermal stability of permafrost subgrades beneath various engineered infrastructures [15]. By facilitating heat exchange with ambient air in cold seasons, these ACSs can cool down and maintain permafrost foundations to protect engineered infrastructures from damage induced by permafrost warming and thawing during climate warming. In cold seasons, CRLs and VDs can enhance the natural ventilation driven by wind pressure and temperature differences. Because convection is a much more efficient heat-transfer mechanism, heat in the underlying permafrost could be transferred into the ambient environment more rapidly [15–18]. A thermosyphon is a heat exchanger that can effectively transfer a heat source to a heat sink through the evaporation and condensation of a working fluid [19]. Because of their superior heat-transfer ability, thermosyphons have been extensively used in the thermal management of a wide range of engineering systems [20–27]. When used for permafrost cooling, thermosyphons generally function in winter and transfer the heat from the evaporation section buried in permafrost to the condensation section exposed in the air [20,22,25]. In the past few decades, these three types of ACSs have been widely used for roadway embankments, airfield runways, oil and gas pipeline systems, buildings and power transmission lines in northern Canada, Alaska, Siberia, and the Qinghai–Tibet Plateau (QTP) [12,13,28–30] (Fig. 1).

The near-surface wind flow (NSWF) is a factor that controls the thermal performance of these ACSs when used in linear transportation infrastructures. The speed and direction of the NSWF determine not only the heat convection type within the CRLs, namely, wind-driven convection or buoyancy-driven convection, but also the intensity of heat convection [16,17,31–34]. Wu et al. [33] studied the cooling mechanisms of the CRL in embankments through distributed temperature measurements within an experimental railway section. The results showed that, in cold seasons, wind-driven convection occurred within the CRL when the ambient wind speed was large, whereas weak buoyancy-driven convection occurred when the ambient wind speed was small. They concluded that the cooling mechanisms and performance of the CRL were controlled by the ambient wind speed and direction. For VDs used for roadway and railway embankments, with a given diameter and a burial height within the embankments, the airflow speed within the duct is closely related to the ambient wind speed and direction [17,35,36]. The NSWF also represents a crucial operating condition for thermosyphons used for permafrost foundation cooling [37,38]. In coupled air–thermosyphon–soil heat transfer systems, the NSWF speed determines the convective heat transfer of the condenser section and hence its heat loss rate during the operation of thermosyphons.

However, to date, field-observed data of NSWFs across engineered infrastructures equipped with ACSs are very scarce. Thus, the wind flow characteristics required to assess the long-term thermal performance of the infrastructure with ACSs were generally assumed based on a prevailing wind direction and a mean or a seasonally varying wind speed [22,25,30,35–43]. These assumptions can result in either over or underestimation of the heat exchange efficiency of the ACSs and hence, unreliable prediction of the permafrost subgrade's long-term thermal regime, which may further lead to an unconservative or uneconomical foundation design.

This article describes systemic field observations of the NSWF across an experimental expressway embankment in the Beiluhe Basin, the central area of the QTP. A total of six meteorological towers were established at both sides of the embankment to collect the NSWF data, including wind speeds at four levels (0.5, 1.5, 3.0, and 4.5 m) above the ground surface and wind directions. Data collection at these observation sites and an adjacent meteorological station serving as a reference was carried out for an entire year. The characteristics of the NSWF across the embankment, including its distribution and seasonal variations, were analyzed based on the
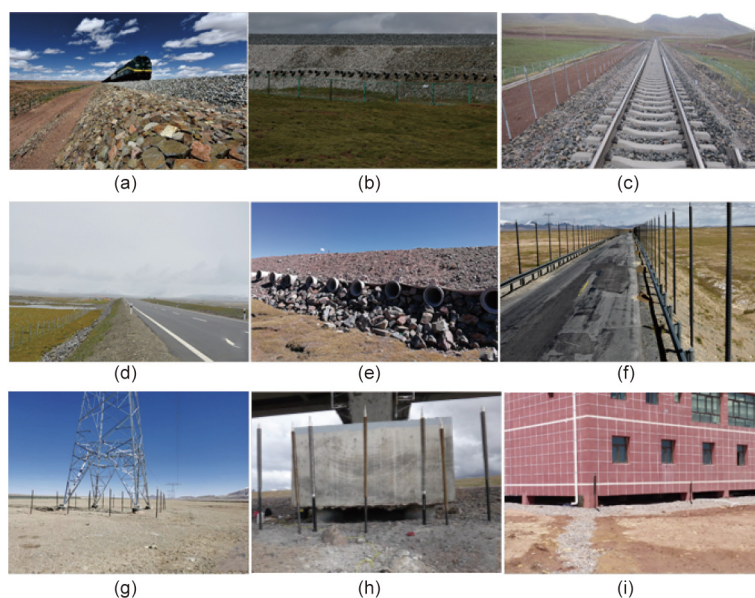
Fig. 1. The individual or combined use of ACSs in a wide range of engineered infrastructures on the QTP: (a) CRLs, (b) CRLs and VDs, and (c) thermosyphons used in railway embankments; (d) CRLs, (e) CRLs and VDs, and (f) thermosyphons used in roadway embankments; and thermosyphons in foundations of (g) power transmission lines, (h) railway bridges, and (i) buildings. The building base was also elevated above the ground surface to promote natural ventilation.

field observed data. Based on field-observed results, the impacts of the wind directions and speed profiles on the thermal performances of the ACSs were discussed. This study's observation data and results will provide an essential scientific basis for the design and maintenance of the ACSs used for linear transportation infrastructure built on the QTP, for example, the existing Qinghai–Tibet Railway and Qinghai–Tibet Highway and the proposed Qinghai–Tibet Expressway.

2. Field site and methods

2.1. Field site

The field site (92°55′36″E, 34°49′21″N) is located in the Beiluhe Basin, the interior of the QTP, as shown in Fig. 2(a). At an elevation of 4618 m above sea level, the local terrain is slightly sloped, with 70%–90% of the ground surface covered by an alpine meadow. The permafrost at the site is predominately continuous, with mean annual ground temperatures at depths of 10–15 m ranging from −0.5 to −1.0 °C. The active layer thickness (the maximum seasonal thaw depth) varies from 2 to 3 m. Ice-rich permafrost layers are encountered immediately beneath the permafrost table based on borehole exploration data. A meteorological station is located approximately 2 km in the northeast direction from the field site. The data from this station show that, from 2003 to 2015, the mean annual air temperature ranged from −2.8 to −4.1 °C and the mean annual precipitation ranged from 230 to 460 mm. Data, including air temperature, wind speed, and wind direction at 2 m above the ground, were collected from July 1, 2018 to June 30, 2019 (referred to as the study period hereafter), at this station to provide a reference in this study.

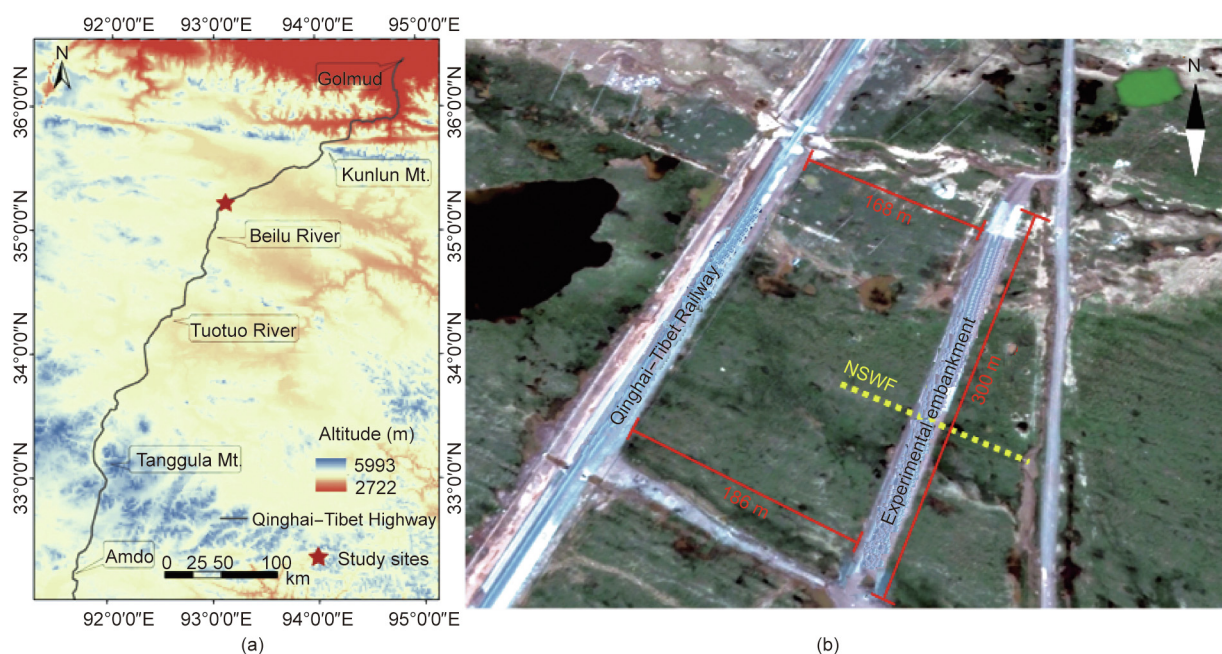### 2.2. Experimental expressway embankment

An experimental expressway embankment with asphalt pavement was built nearly parallel to the Qinghai–Tibet Railway at the field site (refer to Fig. 2(b)) in August 2009 to collect data for constructing expressways in a warm permafrost environment on

the QTP. Various ACSs were included in the embankment to investigate their long-term performances in cooling the underlying permafrost. The experimental embankment has a total length of 300 m, an azimuth angle of 197°, a height of 3 m, a crest width of 13 m, and 1:1.5 side slopes. The embankment was equally divided into ten segments, each 30 m in length. Among them, a single ACS, or a combination of ACSs, including CRLs, VDs, thermosyphons, and hollow concrete brick layers, was installed in nine segments, and the segment without any cooling structures was used as a reference [44].

2.3. Measurement of NSWF

Six meteorological towers were established along a transect perpendicular to the embankment route on both sides of the reference section, as illustrated in Fig. 3. On each side, the distances between the three towers and the embankment slope toe were 0.5, 30, and 60 m, respectively, and as shown in Fig. 3(a), the three towers on the right side (from Golmud to Lhasa, China) were labeled TR-0.5, TR-30, and TR-60, respectively, and those on the left side were TL-0.5, TL-30, and TL-60, respectively. The two towers adjacent to the embankment slope toe (i.e., TR-0.5 and TL-0.5) were 4.5 m tall, and the remaining four (i.e., TR-30, TR-60, TL-30, and TL-60) were 3.0 m tall. The site is relatively flat, and the differences among elevations at the locations of the six towers could be neglected. Considering the prevailing wind direction at the study area and the embankment route, towers TR-60, TR-30, and TR-0.5 were regarded as being on the windward side, whereas TL-60, TL-30, and TL-0.5 were on the leeward side.

Wind speeds and wind directions at six towers were measured by 010C wind-speed sensors and 020C wind-direction sensors, respectively. All sensors were manufactured and calibrated by Met One Instruments, Inc. (USA). The 010C wind-speed sensor uses a lightweight three-cup anemometer to measure the horizontal wind speed. This sensor has a calibrated operating range of 0–50 m·s^{-1}, a resolution of < 0.1 m·s^{-1}, and an accuracy of ±1%. On the 3.0 m tall towers, the three wind-speed sensors were mounted at heights of 0.5, 1.5, and 3.0 m above the ground surface (Fig. 4(a)).

Fig. 2. (a) The location of the field site; (b) an aerial view of the experimental expressway embankment. The distance between the railway and the experimental expressway ranges from 168 to 186 m. Mt.: mountains.
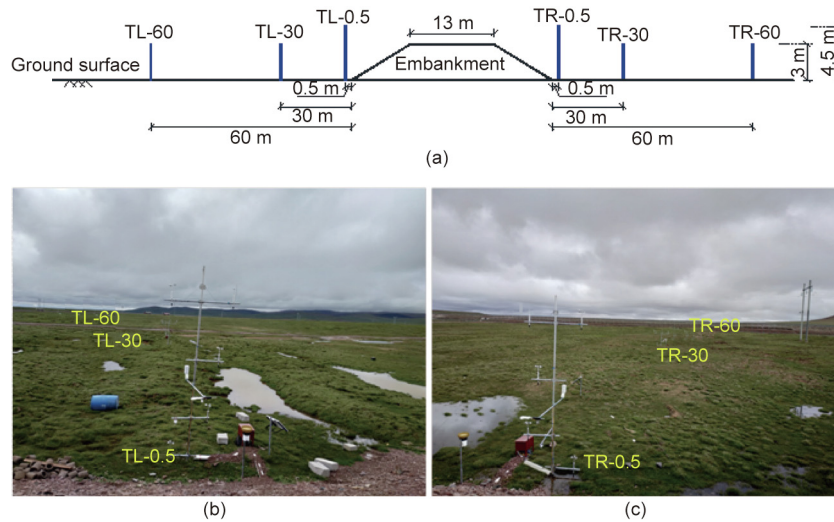
Fig. 3. Deployment of the NSWF observation towers: (a) schematic diagram of the six meteorological tower locations across the embankment and views of the towers on the (b) leeward and (c) windward sides.
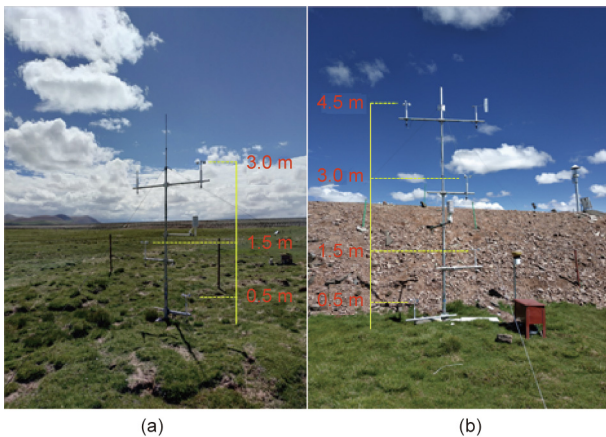
Fig. 4. Wind speed and direction sensors mounted on (a) 3.0 m tall and (b) 4.5 m tall towers.

On the 4.5 m tall towers near the embankment toe, four wind-speed sensors were mounted at heights of 0.5, 1.5, 3.0, and 4.5 m (Fig. 4(b)). On each tower, the 020C wind-direction sensor, with a resolution of < 0.1° and an accuracy of ±3°, was paired with the uppermost wind speed sensor to provide azimuth data (0°–360°) by coupling a lightweight airfoil vane and a single-precision potentiometer. Note that such a sensor is visible on the right end of a horizontal beam in Fig. 4(b). On each side of the embankment, all the sensors were connected to a CR3000 datalogger manufactured and calibrated by Campbell Scientific Inc. (USA) to automatically collect, compute, and store the data at 10 min intervals throughout the study period.

3. Results and analysis

3.1. Characteristics of natural wind flow in the study area

3.1.1. Wind direction

Fig. 5(a) shows the rose diagram of the wind frequency obtained at the meteorological station in the study period. In the study area, west (W), west–southwest (WSW), and west–northwest (WNW) were the prevailing wind directions, and their occurrence frequen-

cies accounted for 18.5%, 14.9%, and 13.0%, respectively, during the study period. The frequencies of the other directions were relatively low, ranging from 0.9% to 8.5%.

The characteristics of the wind directions in cold and warm seasons differed significantly. The cold and warm seasons were determined based on the monthly average air temperature. In the cold season, which was October through April of the following year in this study, the composition of the wind direction was simple (Fig. 5(b)). The frequencies of the three prevailing wind directions, namely, W, WSW, and WNW, were all above 18.5%, with a sum of 65.5%. Following these three directions, the SW winds accounted for 11.5%, and the others were all less than 4.3%. However, in the warm season from May to September, the wind direction was more dispersed (Fig. 5(c)). The peak frequency was less than 12.4%, with four wind directions, namely, east (E), east–northeast (ENE), northeast (NE), and north–northeast (NNE), accounting for 9.6%–12.4%. The frequencies of the other wind directions varied from 1.6% to 8.1%, with a total of 55.4%.

3.1.2. Wind speed and air temperature

As mentioned above, wind speed, air temperature, and their seasonal variations are crucial for the heat transfer processes within the ACSs and the cooling effect on the underlying permafrost subgrade.

Fig. 6 shows the variations in wind speed and air temperature obtained at the meteorological station in the study period. Throughout this period, wind speed varied from 0 to 18 m·s^{-1}, with a mean annual value of 4.4 m·s^{-1}. Air temperature ranged from −26.2 to 17.5 °C, with a mean annual value of −3.6 °C. Both wind speed and air temperature varied seasonally, exhibiting sinusoidal patterns with opposite trends. The wind was stronger in the cold season and weaker in the warm season, which is crucial for applications of ACSs, particularly VDs, for permafrost subgrade cooling on the QTP [13,16,17].

Two indices, mean monthly wind speed (MMWS) and mean monthly air temperature (MMAT), were calculated and are listed in Table 1. From November to March of the following year, MMWSs reached or exceeded 4.8 m·s^{-1}, with a maximum of 7.1 m·s^{-1} in February, while MMATs varied between −14.6 and −9.2 °C. From June to September, MMWSs fell below 3.6 m·s^{-1}, with a minimum of 3.1 m·s^{-1} in September, while MMATs ranged from 3.6 to 7.9 °C.
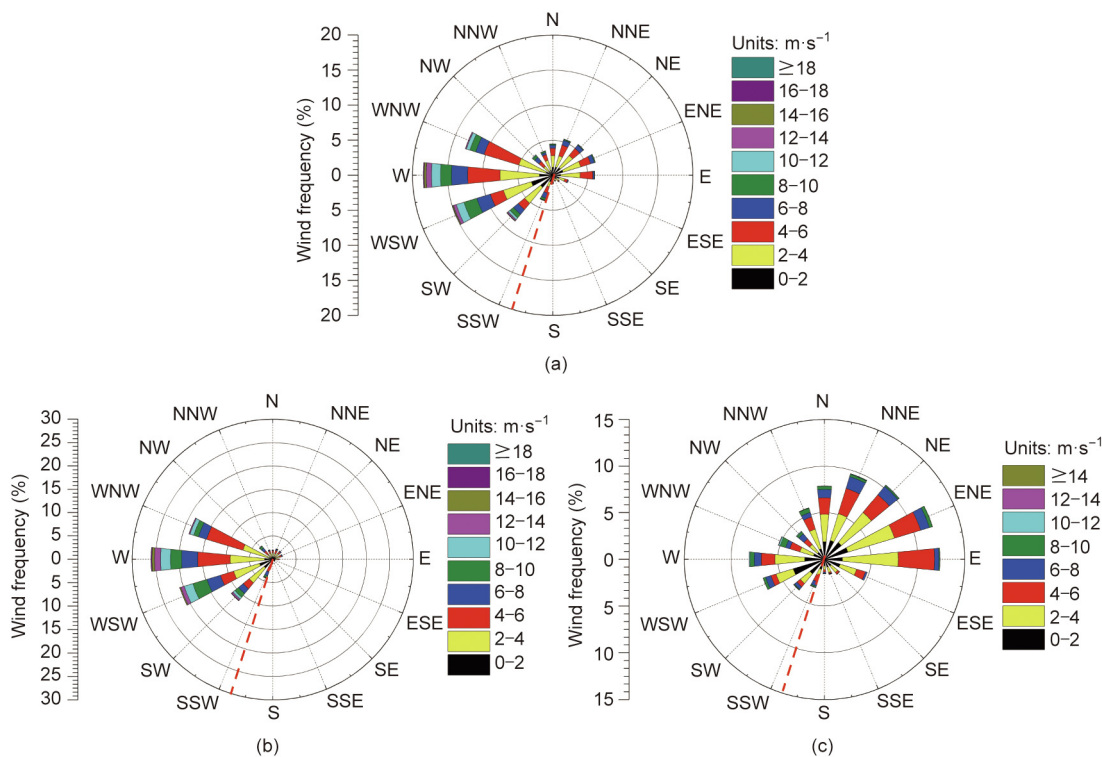
Fig. 5. Rose diagrams of natural wind frequency in the study area during (a) the entire study period, (b) the cold season, and (c) the warm season. The red dotted line represents the embankment route.
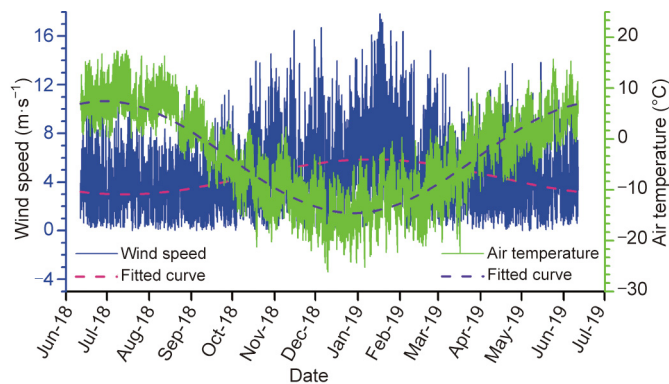

Fig. 6. Variations in wind speed and air temperature in the study period.

Table 1
The mean monthly values of wind speed and air temperature in the study period.

Month	MMWS (m·s⁻¹)	MMAT (°C)
July	3.3	7.9
August	3.4	7.5
September	3.1	3.6
October	3.6	−5.1
November	5.0	−9.2
December	5.6	−13.6
January	5.5	−14.6
February	7.1	−11.2
March	4.8	−9.7
April	4.1	−2.8
May	4.3	0.2
June	3.6	3.6

3.2. Variation in wind direction across the embankment

3.2.1. Observation towers located far from the embankment

Fig. 7 compares the wind rose diagrams for the towers located farthest away from the embankment, namely, TR-60 and TL-60, in the study period. Note that the two towers were located at a distance of 20 times the height of the embankment.

The wind roses in both locations were very close to each other. Specifically, the prevailing winds at TR-60, namely, W, WSW, and WNW, accounted for 17.8%, 15.2%, and 14.1% of the total, respectively, with a sum of 47.1%. In comparison, these three winds at TL-60 represented 18.5%, 13.9%, and 14.6% of the total, respectively, with an aggregate of 47%. Moreover, there is no considerable difference among the three rose charts in Figs. 5(a) and 7, indicating that the existence of an embankment had no meaningful impact on the NSWF direction at a distance of 20 times the embankment height away.

3.2.2. Observation towers located close to the embankment

Figs. 8(a)–(d) show wind rose diagrams at the four towers located relatively close to the embankment (at a distance of ten times of the embankment height or less), namely, TR-30, TL-30, TR-0.5, and TL-0.5, respectively, during the study period.

On the windward side, the prevailing winds were the same as those at TR-60 and TL-60. For instance, Fig. 8(a), the wind rose for TR-30 (ten times the embankment height away), reveals that the three prevailing winds accounted for 18.2%, 14.9%, and 14.5% of the total. In comparison, Fig. 8(c), the wind rose for TR-0.5 (near the embankment toe), shows that the prevailing winds comprised 17.5%, 14.3%, and 14.1% of the total. These values were very close to those at TR-60 and TL-60, suggesting that the embankment's existence did not significantly influence the NSWF directions on the windward side.
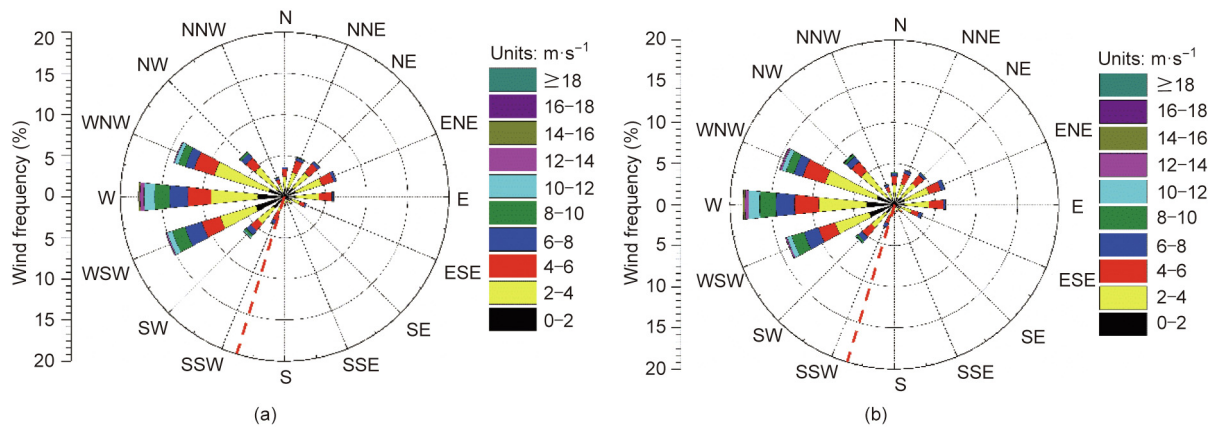
Fig. 7. The wind rose diagrams for (a) TR-60 (windward) and (b) TL-60 (leeward) during the study period. The red dotted line represents the embankment route.
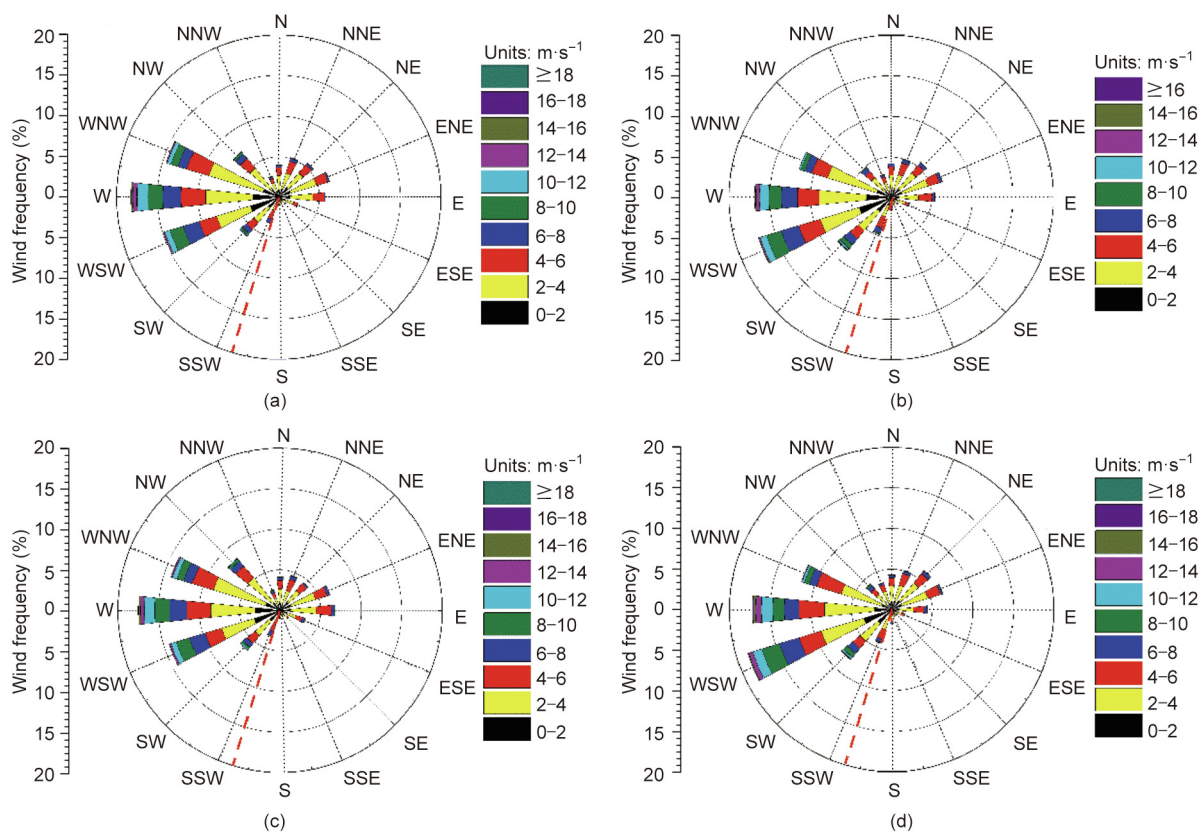

Fig. 8. Wind rose graphs for (a) TR-30, (b) TL-30, (c) TR-0.5, and (d) TL-0.5 during the study period. The red dotted line represents the embankment route.

However, on the leeward side, the wind directions were significantly altered at both TL-30 and TL-0.5. Fig. 8(b) displays that the frequencies of the WSW, W, and WNW winds for TL-30 were 17.2%, 16.8%, and 11.9%, respectively, with the prevailing wind switching from W to WSW. Compared with the wind rose at TL-60 (Fig. 7(b)), the frequency of the WSW wind increased by 3.3%, while the frequency of the WNW wind decreased by 2.7%. The impact on wind directions intensifies as the observation towers are located closer to the embankment. Fig. 8(d) shows that the WSW wind frequency at TL-0.5 reached 18.9%, whereas the WNW wind frequency fell to 11.7%. The results reveal that the embankment itself could significantly alter the NSWF directions within a distance of ten times the embankment height on the leeward side. Apparently, the embankment

obstructed the winds perpendicular to its course and facilitated those parallel to its course.

3.3. Variation in wind speed across the embankment

Fig. 9 exhibits the variations in MMWS at heights of 0.5, 1.5, and 3.0 m along the six towers in the study period. The seasonal variations in all MMWSs were synchronous with their values, generally reaching their respective maximum values in February and falling to their minimum in September. However, the embankment clearly impacted the wind speeds, especially for the two towers close to the slope toe, namely, TR-0.5 and TL-0.5. The closer to the ground surface it is, the greater the embankment influence on the NSWF speed is.
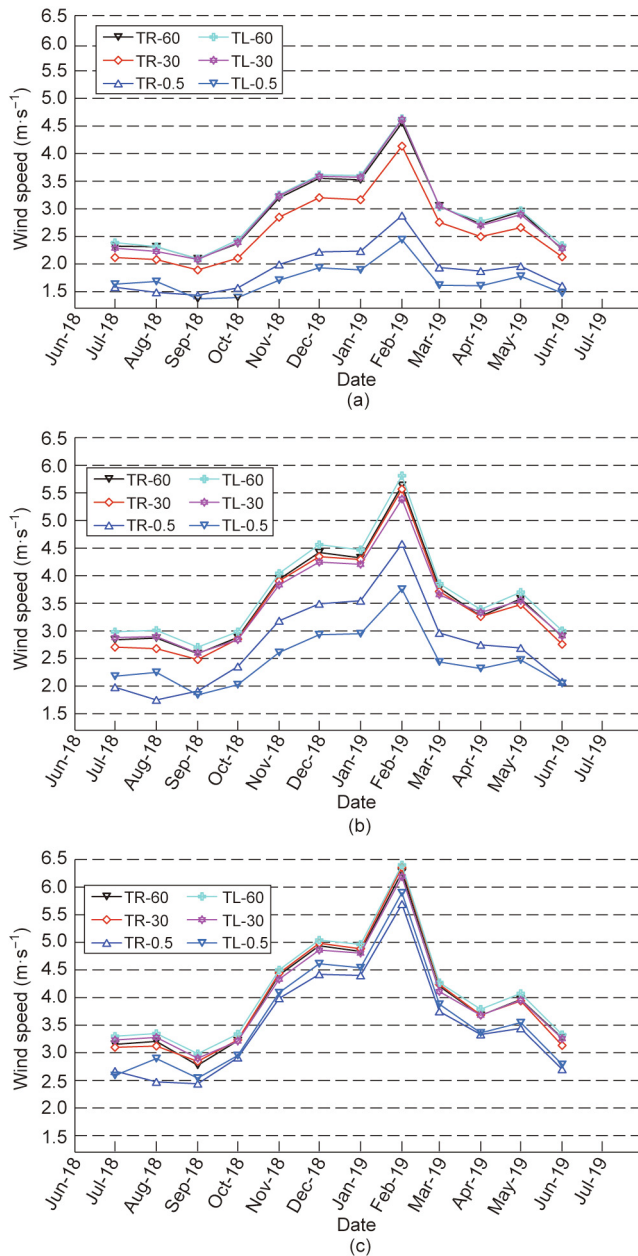
Fig. 9. Variations in the MMWS at heights of (a) 0.5 m, (b) 1.5 m, and (c) 3.0 m along the six towers in the study period.

and the rest (i.e., TR-60, TR-30, TL-60, and TL-30) were still significant. For example, the MMWS values at TR-0.5 were 0.8–1.5 m·s^{-1} smaller than those at the other four locations. When the observation height reached 3.0 m (Fig. 9(c)), the MMWS data differences at all six towers in the same month were within 0.7 m·s^{-1}.

Notably, at 0.5 and 1.5 m, the MMWS values at TR-0.5 were generally greater than those at TL-0.5, except for July and August. As seen from Fig. 5(c), the prevailing wind during the warm season switched from W to E, rendering TL-0.5 on the windward side and TR-0.5 on the leeward side, and hence, the MMWSs values were higher at TL-0.5 in these two summer months. However, the MMWS values at 3.0 m at TL-0.5 were slightly but consistently greater than those at TR-0.5 throughout the study period. The considerable differences in the MMWS at 0.5 and 1.5 m above the ground surface along the six towers clearly illustrated the embankment's obstruction effect on the NSWF.

Fig. 10 compares MMWS at a height of 4.5 m along TR-0.5 and TL-0.5 in the study period. At this height, the MMWS values at the two locations were very close throughout the study period. In the summertime, the MMWS values at the two locations were almost identical. In contrast, in the cold season, the MMWS values at TL-0.5 were marginally greater than those at TR-0.5. This result can be explained by the acceleration of wind flow when it passes over the embankment. The seasonal variations in the MMWS differences between the two locations can be attributed to the more consistent prevailing winds during the cold season and the more dispersed winds during the warm season in the study area.

3.4. Wind speed profiles across the embankment

As mentioned above, the NSWF speed is one of the main factors affecting the thermal performance of ACSs used in permafrost subgrade cooling. However, the conventional practice uses wind data measured at a given height, for example, 10 m, from a weather station. A power law is typically applied to interpolate wind speeds at various heights above the ground surface for engineering applications because of its simplicity [45–47]. The power law is described as follows:

$$y = v_{10}\left(\frac{x}{10}\right)^a \tag{1}$$

where y and v_{10} are the wind speeds at heights of x and 10 m above the ground surface, respectively, and a is the power-law index (PLI). The value of the PLI is considered to be a constant that depends on ground roughness.

The MMWS data in February and September from the six towers were analyzed to examine the impact of existing structures,

At the 0.5 m height, the MMWS values at TR-60, TL-60, TR-30, and TL-30 shown in Fig. 9(a) were close. Among the four towers, the MMWS values at TR-30 in the study period were approximately 0.2–0.3 m·s^{-1} lower than those of the rest. At the observation location near its slope toe, the embankment significantly slowed the wind, particularly on the leeward side. On the windward side, the maximum MMWS at TR-0.5 was 1.8 m·s^{-1} or 40% smaller than that of TR-60. However, on the leeward side, the peak MMWS at TL-0.5 was 2.2 m·s^{-1} or 50% lower than that of TL-60.

The embankment impact on the wind speeds appeared to decrease with an increasing observation height. At 1.5 m above the ground surface, Fig. 9(b) shows that the MMWS data at TR-60, TR-30, TL-60, and TL-30 almost overlapped throughout the entire study period. However, the differences between the two towers near the embankment slope toe (i.e., TR-0.5 and TL-0.5)
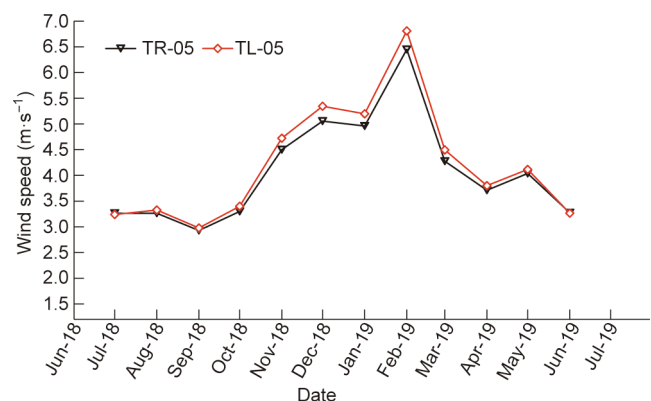

Fig. 10. Variations in the MMWS at a height of 4.5 m along TR-0.5 and TL-0.5 in the study period.

such as an embankment, on the wind speed profiles. The v_{10} values for February and September obtained from the nearby weather station were 8.6 and 3.4 $m \cdot s^{-1}$, respectively. Figs. 11(a)–(d) depict the wind speed profiles at TR-60, TL-60, TR-30, and TL-30. At the four locations, the wind speed variations with increasing height could be well fitted using the power law. However, the PLI values varied considerably with the location and the season. Among the four observation towers, the PLI values in September varied between

0.14 and 0.18, whereas the PLI values in February were greater, ranging from 0.21 to 0.24.

Fig. 12 compares the wind speed profiles at TR-0.5 and TL-0.5, which are closest to the embankment and therefore directly affect the ACSs' performance. The results show that even though the wind speeds near the embankment slope toe were considerably affected (refer to Figs. 9 and 10), the wind speed profiles can still be described by the power law. However, the PLI values at the
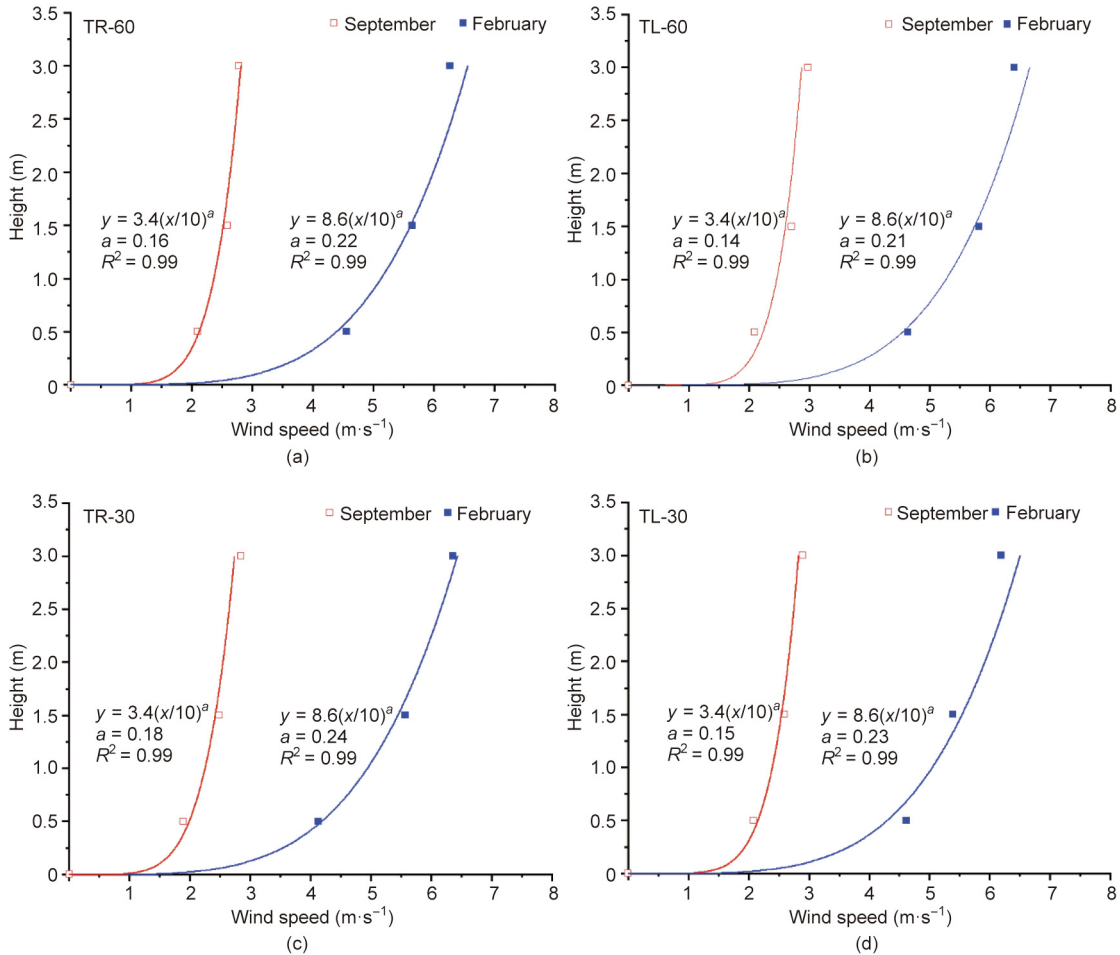

Fig. 11. Wind speed profiles at (a) TR-60, (b) TL-60, (c) TR-30, and (d) TL-30 in September and February and fitted curves using the power law. R^2: correlation coefficient.
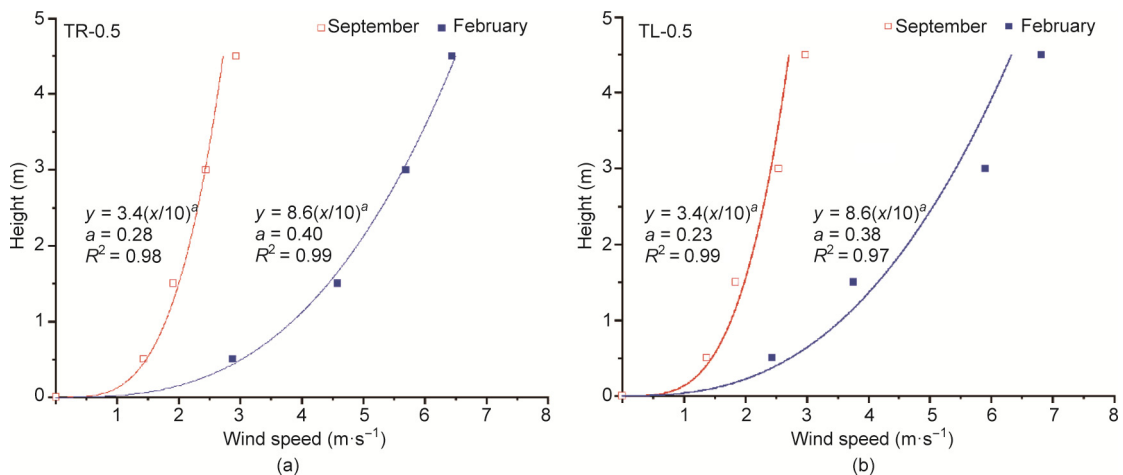

Fig. 12. Wind speed profiles at (a) TR-0.5 and (b) TL-0.5 in September and February and fitted curves using the power law.

two locations were significantly greater than those at the four towers farther away from the embankment as discussed above. The PLI values at TR-0.5 and TL-0.5 reached 0.28 and 0.23 in September and jumped to 0.40 and 0.38 in February, respectively. These substantially greater PLI values at the two towers clearly reflect the embankment's accelerating effect on the ambient wind flow.

To quantify the spatial and temporal variations in the PLI values of wind speed profiles across the embankment, Fig. 13 shows the fitted PLI values at TR-60, TR-30, TL-60, and TL-30 during the entire study period. The figure shows the seasonal variations in the PLIs are synchronous and significant. The PLI values are smaller for lower wind speeds in the warm season and larger for higher wind speeds in the cold season, consistent with observations from urban terrains [45–47]. Additionally, the PLI values on the windward side towers are slightly greater than those on the leeward side at the same distance from the embankment in the same month.

The PLI values at 60 m away from the embankment in the cold season ranged from 0.18 to 0.23, with an average of 0.21, whereas the values in the warm season varied from 0.13 to 0.22, with an average of 0.16. At 30 m away from the embankment, the PLI values increase slightly, with an average PLI rising to 0.25 in the cold season and to 0.18 in the warm season. Among the four locations, through the year, only a few PLI values were being smaller than 0.16, which was typically used in previous numerical evaluations of the long-term thermal performances of ACSs used in engineered infrastructures on the QTP [16,22,25,27,30,35–43].
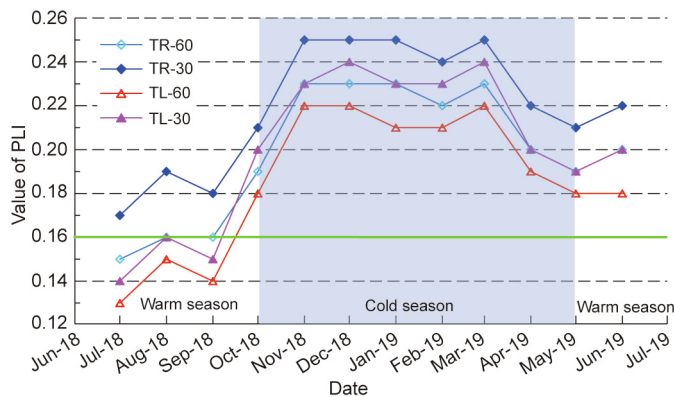
Fig. 13. NSWF PLI at TR-60, TR-30, TL-60, and TL-30 in the study period.

4. Discussion

4.1. Significance of the NSWF speed profile to the long-term thermal performances of ACSs

A reliable evaluation of the long-term thermal performances of ACSs is essential for the design and maintenance of engineered infrastructures built in a permafrost environment. In numerical evaluations, the NSWF speed is a crucial boundary condition for the heat exchange between the ACSs and ambient air. As mentioned previously, the wind speed observed at a 10 m height is generally used to determine the NSWF speed according to a power law, and the two PLI values (i.e., 0.12 and 0.16) were typically used in previous numerical evaluations of the long-term thermal performances of ACSs used in engineered infrastructures on the QTP [16,22,25,27,30,35–43]. However, the field-observed data in this study showed that the PLI not only varied considerably with wind speed but also substantially exceeded the assumed values (Fig. 11).

The mean annual wind speed (MAWS) values at three heights (0.5, 1.5, and 3.0 m) along TR-60 and TL-60 were analyzed to quantify the PLI values on an annual basis in the study period, as shown in Fig. 14. The fitted results showed that the annual average PLI value was 0.19. In the figure, the power-law predicted wind speed profiles with v_{10} from the reference meteorological station and PLI values of 0.12 and 0.16 were also plotted for comparison. The NSWF speed values estimated using previous PLI values are considerably greater than the field-observed values. For instance, the wind speed is overestimated by 12%–25% and 5%–13% at 0.5 and 1.5 m above the ground surface, respectively. At a height of 3.0 m, the predicted wind speed with a PLI of 0.12 would still be overvalued by 10%.

In permafrost regions on the QTP, most of the railway and roadway embankments are generally under 5 m in height [48,49], meaning that most numerical evaluations of the long-term thermal performances of embankments constructed with ACSs, including CRLs, VDs, and thermosyphons, applied overrated NSWF speeds; these overrated speeds led to an overestimated ACS heat-exchange efficiency and hence an unconservative assessment of their long-term permafrost cooling effects. For example, an overestimated NSWF speed would result in an overrated airflow speed within VDs and an inflated heat extraction rate for thermosyphons. More importantly, for CRLs used in railway and roadway embankments, an overestimated NSWF speed may not only erroneously determine the convection type, namely, wind-driven versus buoyancy-driven, but also, the convection intensity within the
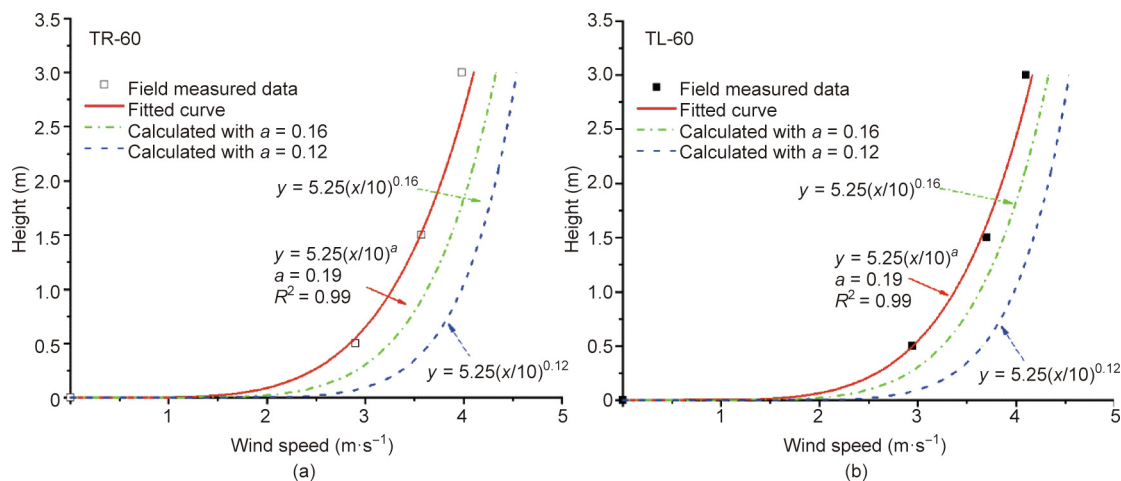

Fig. 14. Observed mean annual wind speed profiles along (a) TR-60 and (b) TL-60 and the power-law predicted profiles with PLI values of 0.12 and 0.16.

CRLs. The overvalued heat-exchange efficiency of these ACSs would lead to insufficient designs of these ACSs, which may jeopardize the long-term thermal stability of the permafrost subgrade.

4.2. Significance of the NSWF direction on the long-term thermal performances of ACSs

The NSWF direction is also a vital factor affecting the long-term thermal performances of the CRLs and VDs used in linear transportation infrastructures. Taking a roadway embankment with VDs as an example, the NSWF direction, together with the embankment route azimuth, determines the angle between the NSWF and the duct axis, and hence, determines the relationship between the environmental wind speed and the duct airflow speed.

The field-observed data on two days, namely, August 15 and December 15 of 2018, were selected to represent the duct airflow conditions in warm and cold seasons, respectively. Fig. 15 shows the half-hour average environmental wind speed and airflow speed within a duct in the experimental expressway embankment. The duct has an inner diameter of 0.4 m and is buried at a height of 1.0 m above the ground surface. The environmental wind speed data were collected from the weather station at a height of 2 m, and the airflow speed data were measured by an ultrasonic anemometer installed along the duct axis. Fig. 16 illustrates the half-hour average environmental wind direction on the two selected days. On December 15, the environmental wind direction was relatively persistent, ranging from 242° to 332°, with a daily average of 282°, which is roughly perpendicular to the embankment route (197°). On this day, there was a clear positive correlation between the environmental wind speed and the duct airflow speed, with the latter reaching a maximum of 5.3 m·s^{-1}. On the other hand, the environmental wind direction on August 15 varied greatly, ranging from 4° to 360°. For instance, the environmental wind direction at 18:00 was nearly perpendicular to the embankment route or almost parallel to the duct axis, resulting in a duct airflow speed of 2.1 m·s^{-1}, which was about half of the environmental wind speed (4.3 m·s^{-1}). However, the environmental wind direction at 21:30 was approximately parallel to the embankment route or almost perpendicular to the duct axis, generating a duct airflow speed of only 0.2 m·s^{-1}, which accounts for approximately 1/30 of the environmental wind speed (6.8 m·s^{-1}).

These results demonstrate that both the environmental wind direction and speed need to be considered in evaluating the long-term thermal performance of linear transportation infrastructure with ACSs. An overestimation of the ACS heat-exchange efficiency would likely occur otherwise. However, most existing numerical simulations [16,22,25,27,30,35–43] ignored wind direction variations due to their complexities. Fortunately, the wind

direction on the QTP in wintertime is relatively persistent (Fig. 5(b)), which instills confidence in assuming a predominant wind direction in numerical simulations. Regarding engineering applications, the angle between the actual environmental wind direction and the route of linear transportation infrastructure should be considered in the design of VDs. For example, if the prevailing wind direction is close to the route of roadway embankment, thermosyphons or CRLs would be a better choice than VDs for permafrost subgrade cooling. Otherwise, the VDs should be aligned with the prevailing wind direction in the cold season as much as possible.

5. Conclusions

The NSWF is crucial in determining the heat-exchange efficiency of the ACSs used for permafrost subgrade cooling. This study focuses on NSWF across linear transportation infrastructures in a high-altitude permafrost environment. A yearlong field observation of the NSWF across an embankment located in the interior of the QTP, including the observation system layout, measurement methods, and collected data, was described. Based on the field-observed data, the environmental air and wind characteristics, wind direction and speed from both the windward and leeward sides of the embankment, and their variations with varying distances from the embankment were analyzed. Furthermore, the significance of the NSWF to the thermal performance of ACSs, including CRLs, VDs, and thermosyphons, was discussed in the context of linear transportation infrastructure. The following conclusions were obtained from the field observations, analyses, and discussion:

(1) The wind direction in the cold season at the study site was relatively persistent. The occurrence frequencies of W, WNW, and WSW winds each accounted for more than 18.5%, with a sum of 65.5%. In contrast, the wind direction in the warm season was considerably more dispersed, with no single wind direction exceeding 15% in its occurrence frequency. The wind speed in the cold winter was substantially higher than that in the warm summer. The ACSs can significantly benefit from cold winds in the cold season to preserve the permafrost subgrade.

(2) The embankment's existence did not impact the wind direction on the windward side. However, the wind perpendicular to the embankment course on the leeward side was slowed, and that parallel to the embankment course was accelerated. The embankment obstructed the wind and resulted in a considerable decrease in wind speed at elevations lower than its height on both the windward and leeward sides. Above the embankment crest, the wind speed on the leeward side was enhanced. The NSWF speed could recover at approximately 15–20 times the embankment height.
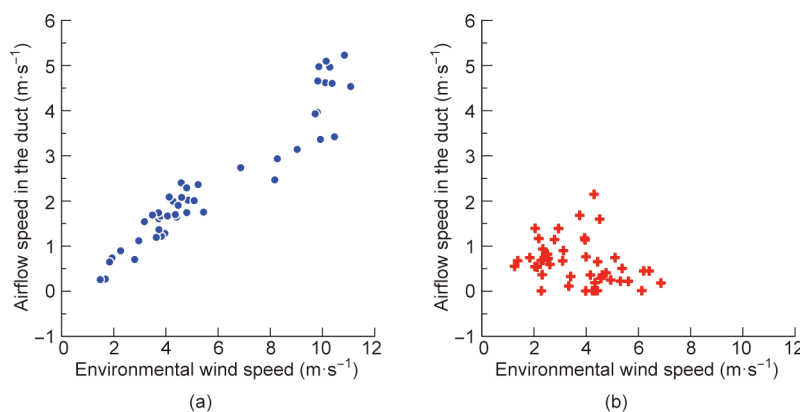

Fig. 15. Environmental wind speed versus duct airflow speed on (a) December 15 and (b) August 15 of 2018.
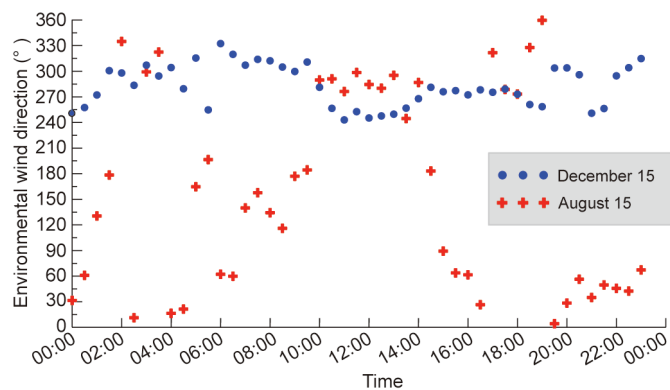
Fig. 16. Environmental wind direction on (a) December 15 and (b) August 15 of 2018.

(3) The wind speed profiles across the embankment can be fitted well with a power law. The PLI values changed considerably with the seasonally varied wind speed and distance from the embankment. At locations 20 times the embankment height away, the average PLI was 0.21 in wintertime and 0.16 in summertime. On an annual basis, the PLI value was 0.19, which was significantly larger than the values (e.g., 0.12 and 0.16) used in previous numerical simulations. The underestimation of the PLI in these numerical simulations would lead to an overestimated heat-exchange efficiency of the ACSs and, therefore, an unconservative design for permafrost subgrade cooling.

(4) The wind direction is also a crucial factor affecting the thermal performances of the CRLs and VDs commonly used in linear transportation infrastructures. Ignoring the wind direction variations would also yield an overrated heat-exchange efficiency and an unconservative design. It is highly recommended that the angle between the prevailing environment wind direction and the linear transportation infrastructure route be considered in the design of VDs.

The presented results are obtained from one case, and more field observations on different settings are needed. Factors including ground surface conditions, landforms, the geometry of embankment have a significant impact on the characteristics of the NSWF across an expressway embankment and should be considered when applying the results or selecting future field observation sites.

Acknowledgment

Compliance with ethics guidelines

Yanhu Mu, Wei Ma, Zhaohui (Joey) Yang, Xiaolin Li, Kun Zhang, and Yuncheng Mao declare that they have no conflict of interest or financial conflicts to disclose.

References

[1] Gruber S. Derivation and analysis of a high-resolution estimate of global permafrost zonation. Cryosphere 2012;6(1):221–33.
[2] Hossain K. Arctic melting: a new economic frontier and global geopolitics. Curr Dev Arct Law 2017;5:40–5.
[3] Chong ZR, Yang SHB, Babu P, Linga P, Li XS. Review of natural gas hydrates as an energy resource: prospects and challenges. Appl Energy 2016;162:1633–52.
[4] Nelson FE, Anisimov OA, Shiklomanov NI. Climate change and hazard zonation in the circum-arctic permafrost regions. Nat Hazards 2002;26(3):203–25.
[5] Instanes A, Anisimov O, Brigham L, Goering D, Khrustalev LN, Ladanyi B, et al. Infrastructure: buildings, support systems, and industrial facilities. In: Arctic climate impact assessment. New York: Cambridge University Press; 2005. p. 907–44.
[6] Larsen P, Goldsmith S, Smith O, Wilson M, Strzepek K, Chinowsky P, et al. Estimating future costs for Alaska public infrastructure at risk from climate change. Glob Environ Change 2008;18(3):442–57.
[7] Wu QB, Niu FJ. Permafrost changes and engineering stability in Qinghai–Xizang Plateau. Chin Sci Bull 2013;58(10):1079–94.
[8] Ma W, Niu FJ, Mu YH. Basic research on the major permafrost projects in the Qinghai-Tibet Plateau. Adv Earth Sci 2012;11(27):1185–91. Chinese.
[9] Streletskiy DA, Suter LJ, Shiklomanov NI, Porfiriev BN, Eliseev DO. Assessment of climate change impacts on buildings, structures and infrastructure in the Russian regions on permafrost. Environ Res Lett 2019;14(2):025003.
[10] Suter L, Streletskiy D, Shiklomanov N. Assessment of the cost of climate change impacts on critical infrastructure in the circumpolar Arctic. Polar Geogr 2019;42(4):267–86.
[11] Hjort J, Karjalainen O, Aalto J, Westermann S, Romanovsky VE, Nelson FE, et al. Degrading permafrost puts Arctic infrastructure at risk by mid-century. Nat Commun 2018;9(1):5147.
[12] Andersland OB, Ladanyi B. Frozen ground engineering. 2nd ed. New York City: John Wiley & Sons, Inc.; 2003.
[13] Ma W, Cheng GD, Wu QB. Construction on permafrost foundations: lessons learned from the Qinghai–Tibet Railroad. Cold Reg Sci Technol 2009;59 (1):3–11.
[14] Bommer C, Phillips M, Arenson LU. Practical recommendations for planning, constructing and maintaining infrastructure in mountain permafrost. Permafr Periglac Process 2010;21(1):97–104.
[15] Goering DJ, Kumar P. Winter-time convection in open-graded embankments. Cold Reg Sci Technol 1996;24(1):57–74.
[16] Cheng GD, Lai YM, Sun ZZ, Jiang F. The 'thermal semi-conductor' effect of crushed rocks. Permafr Periglac Process 2007;18(2):151–60.
[17] Niu FJ, Cheng GD, Xia HM, Ma LF. Field experiment study on effects of duct-ventilated railway embankment on protecting the underlying permafrost. Cold Reg Sci Technol 2006;45(3):178–92.
[18] Chataigner Y, Gosselin L, Doré G. Optimization of embedded inclined open-ended channel in natural convection used as heat drain. Int J Therm Sci 2009;48(6):1151–60.
[19] Jafari D, Franco A, Filippeschi S, Di Marco P. Two-phase closed thermosyphons: a review of studies and solar applications. Renew Sustain Energy Rev 2016;53:575–93.
[20] Wu J, Ma W, Sun Z, Wen Z. In-situ study on cooling effect of the two-phase closed thermosyphon and insulation combinational embankment of the Qinghai–Tibet Railway. Cold Reg Sci Technol 2010;60(3):234–44.
[21] Chotivisarut N, Nuntaphan A, Kiatsiriroat T. Seasonal cooling load reduction of building by thermosyphon heat pipe radiator in different climate areas. Renew Energy 2012;38(1):188–94.
[22] Mu Y, Li G, Yu Q, Ma W, Wang D, Wang F. Numerical study of long-term cooling effects of thermosyphons around tower footings in permafrost regions along the Qinghai–Tibet Power Transmission Line. Cold Reg Sci Technol 2016;121:237–49.
[23] Ersöz MA. Effects of different working fluid use on the energy and exergy performance for evacuated tube solar collector with thermosyphon heat pipe. Renew Energy 2016;96:244–56.
[24] Yan C, Shi W, Li X, Wang S. A seasonal cold storage system based on separate type heat pipe for sustainable building cooling. Renew Energy 2016;85: 880–9.
[25] Pei WS, Zhang MY, Lai YM, Yan ZR, Li SY. Evaluation of the ground heat control capacity of a novel air-L-shaped TPCT-ground (ALTG) cooling system in cold regions. Energy 2019;179(15):655–68.
[26] Junior AAM, Mantelli MBH. Thermal performance of a novel flat thermosyphon for avionics thermal management. Energy Convers Manag 2019;202:112219.
[27] Li X, Li J, Zhou G, Lv L. Quantitative analysis of passive seasonal cold storage with a two-phase closed thermosyphon. Appl Energy 2020;260:114250.
[28] Esch DC. Road and airfield design for permafrost conditions. In: Vinson TS, Rooney JW, Haas WH, editors. Roads and airfields in cold regions: a state of the practice report. New York City: American Society of Civil Engineers; 1996. p. 121–49.
[29] Doré G, Niu F, Brooks H. Adaptation methods for transportation infrastructure built on degrading permafrost. Permafr Periglac Process 2016;27(4):352–64.
[30] Mu YH, Li GY, Ma W, Song ZM, Zhou ZW, Wang F. Rapid permafrost thaw induced by heat loss from a buried warm-oil pipeline and a new mitigation measure combining seasonal air-cooled embankment and pipe insulation. Energy 2020;203:117919.
[31] Zhang MY, Lai YM, Yu WB, Zhang JM. Contrast experimental study on cooling effect and mechanism between closed and open riprapped-embankment. Chin J Rock Mech Eng 2005;24(15):2671–7. Chinese.
[32] Zhang M, Lai Y, Li S, Zhang S. Laboratory investigation on cooling effect of sloped crushed-rock revetment in permafrost regions. Cold Reg Sci Technol 2006;46(1):27–35.
[33] Wu QB, Cheng HB, Jiang GL, Ma W, Liu YZ. Cooling mechanism of embankment with block stone interlayer in Qinghai–Tibet railway. Sci China Ser E 2007;50 (3):319–28.

[34] Qian J, Yu QH, You YH, Hu J, Guo L. Analysis on the convection cooling process of crushed-rock embankment of high-grade highway in permafrost regions. Cold Reg Sci Technol 2012;78:115–21.

[35] Zhang M, Lai Y, Niu F, He S. A numerical model of the coupled heat transfer for duct-ventilated embankment under wind action in cold regions and its application. Cold Reg Sci Technol 2006;45(2):103–13.

[36] Li XY, Yu QH, You YH, Guo L. Study of air flow characteristics in ventilation duct of ventilated embankment. J Glaciol Geocryol 2016;38(5):1300–7. Chinese.

[37] Zhang M, Lai Y, Zhang J, Sun Z. Numerical study on cooling characteristics of two-phase closed thermosyphon embankment in permafrost regions. Cold Reg Sci Technol 2011;65(2):203–10.

[38] Pei W, Zhang M, Li S, Lai Y, Long J, Zhai W, et al. Geotemperature control performance of two-phase closed thermosyphons in the shady and sunny slopes of an embankment in a permafrost region. Appl Therm Eng 2017;112:986–98.

[39] Sun B, Yang L, Liu Q, Xu X. Numerical modelling for crushed rock layer thickness of highway embankments in permafrost regions of the Qinghai–Tibet Plateau. Eng Geol 2010;114(3–4):181–90.

[40] Lebeau M, Konrad JM. Non-Darcy flow and thermal radiation in convective embankment modeling. Comput Geotech 2016;73:91–9.

[41] Yu W, Liu W, Chen L, Yi X, Han F, Hu D. Evaluation of cooling effects of crushed rock under sand-filling and climate warming scenarios on the Tibet Plateau. Appl Therm Eng 2016;92:130–6.

[42] Liu M, Ma W, Niu F, Luo J, Yin G. Thermal performance of a novel crushed-rock embankment structure for expressway in permafrost regions. Int J Heat Mass Transf 2018;127(B):1178–88.

[43] Hou YD, Wu QB, Wang KG, Ye ZG. Numerical evaluation for protecting and reinforcing effect of a new designed crushed rock revetment on Qinghai–Tibet Railway. Renew Energy 2020;156:645–54.

[44] Gu W, Yu QH, Qian J, Jin HJ, Zhang JM. Qinghai–Tibet expressway experimental research. Sci Cold Arid Reg 2010;2(5):396–404.

[45] Hussain M. Dependence of power law index on surface wind speed. Energy Convers Manag 2002;43(4):467–72.

[46] Lim J, Ooka R, Kikumoto H. Effect of diurnal variation in wind velocity profiles on ventilation performance estimates. Energy Build 2016;130:397–407.

[47] Kikumoto H, Ooka R, Sugawara H, Lim J. Observational study of power-law approximation of wind profiles within an urban boundary layer for various wind conditions. J Wind Eng Ind Aerodyn 2017;164:13–21.

[48] Mu Y, Ma W, Niu F, Liu Y, Fortier R, Mao Y. Long-term thermal effects of air convection embankments in permafrost zones: case study of the Qinghai–Tibet Railway, China. J Cold Reg Eng 2018;32(4):05018004.

[49] Chai M, Mu Y, Zhang J, Ma W, Liu G, Chen J. Characteristics of asphalt pavement damage in degrading permafrost regions: case study of the Qinghai–Tibet Highway, China. J Cold Reg Eng 2018;32(2):05018003.